Supplement of Atmos. Chem. Phys., 16, 2843–2862, 2016
http://www.atmos-chem-phys.net/16/2843/2016/
doi:10.5194/acp-16-2843-2016-supplement

Atmospheric Chemistry and Physics Open Access
EGU

Supplement of

Climatic impacts of stratospheric geoengineering with sulfate, black carbon and titania injection

Anthony C. Jones et al.

Correspondence to: Anthony C. Jones (aj247@exeter.ac.uk)

Section S1. Representation of gravitational sedimentation rates for aerosol species

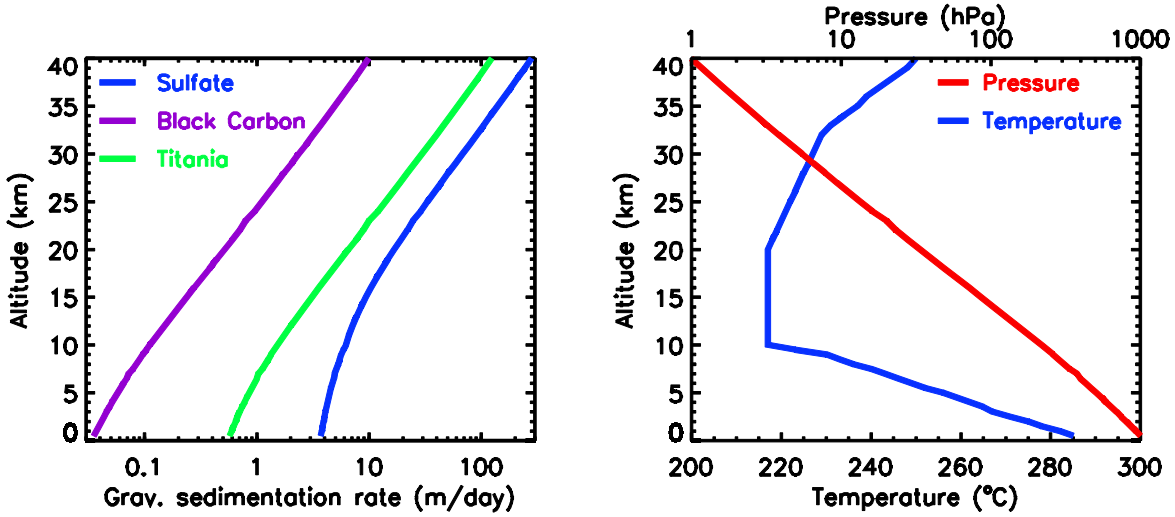

Figure S1. *(left) Gravitational sedimentation rates for sulfate, titania and black carbon, calculated using densities of 1769, 4230 and 1000 kg/m^3 respectively, the mass-weighted radii of the specified log-normal distributions and the method of Pruppacher & Klett (1979) (right) We use the International Standard Atmosphere (ICAO, 1993) for temperature and pressure as a function of altitude*

Text S1. This plot shows the gravitational sedimentation rates for the different aerosol species, based on the size-distributions and aerosol densities given within the manuscript and the caption.

Section S2. Description of the method used for conducting the simulations

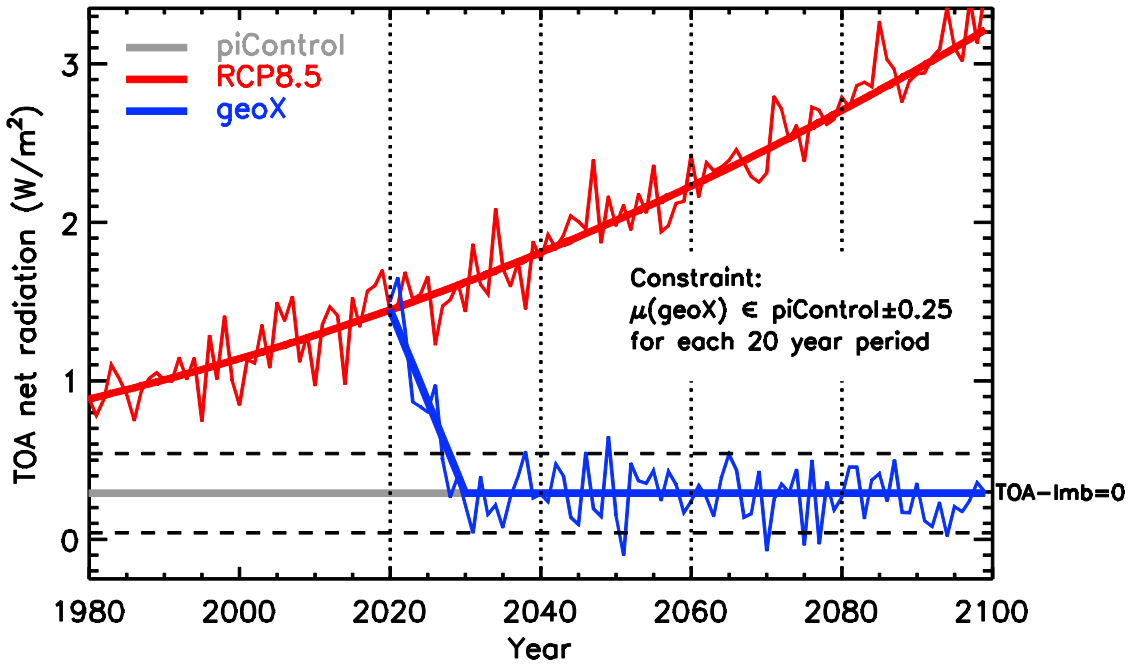

Figure S2. *Schematic showing the goal of the geoengineering strategy*

We firstly define the top of the atmosphere net radiation imbalance (*TOA-Imb*), and then explain how the simulations were conducted. To calculate the TOA-Imb for a certain simulation, we calculate the TOA net radiation (incoming SW minus outgoing LW+SW) and average this annually and globally (denote this value *R(t)* where *t* refers to the year). Next we do the same for each year of the 240-year pre-industrial control (piControl) simulation. We then average the piControl values to obtain the net radiative imbalance of the piControl simulation (denote this *C*, equal to 0.29 W/m^2). The TOA-Imb for year *t* is calculated as *R(t)* – *C*. For this simulation, we aim to achieve TOA-Imb=0 via sufficient aerosol injection (Fig. S2).

We now describe the simulation timeline. The RCP8.5 simulations had already been conducted prior to this investigation as part of CMIP5. The geoengineering simulations took place in 3 phases: (a) we performed atmosphere-only simulations of 1Tg/yr aerosol injection to determine the aerosol TOA radiative effect; (b) we used the aerosol radiative effect to calculate initial injection rate estimates; (c) we began the 80-year GCM integrations, calibrating the injection rates en route

a. We performed atmosphere-only simulations with a constant 1 Tg/yr aerosol injection rate using historical background-conditions (1990-2005). We then determined the steady-state annual/global-mean aerosol radiative effect (the difference in TOA net radiation between the aerosol simulation and the control, per injection rate), which is given in the following table. For sulfate, because the radiative effect was small, we performed an additional simulation with 5Tg[SO_2]/yr and then divided the results by 5 for precision. Similarly, the

black carbon simulation failed to converge to steady state within 15 years and was therefore run for a further 15 years.

Table S1	Sulfate	Titania	Black Carbon
TOA radiative effect (Wm^{-2} / Tg yr^{-1})	0.46	1.1	7.4

Table S1. *TOA radiative effect per injection rate*

b. Rather than use the TOA-Imb from the RCP8.5 simulations to estimate the required aerosol injection rates, we instead used the Anthropogenic Radiative Forcing (ARF), which was acquired from http://www.pik-potsdam.de/~mmalte/rcps/ (see Meinshausen et al, 2011). Specifically, we deducted the 1860 ARF (0.17 W/m^2) from the ARFs for 2020, 2040, 2060, 2080, and 2100, and then calculated the injection rates required to offset these adjusted ARFs by dividing by the TOA aerosol radiative effect. Because each model will have an ARF which is different from Meinshausen et al (2011) it is possible that our initial estimate is in error. However, our method uses this only as an initial 1st guess for the injection rates, which are iteratively adjusted as described in c). The model then linearly interpolates the injection rates between these years.

Table S2	Anthro-RF (Wm^{-2})		SO_2 injection rate (Tg/yr)		Titania injection rate (Tg/yr)		BC injection rate (Tg/yr)	
Year	Actual	Adjusted	Initial	Final	Initial	Final	Initial	Final
2020	2.56	2.39	5.2	4.4	2.2	1.4	0.32	0.21
2040	3.83	3.66	8.0	7.4	3.3	2.5	0.49	0.29
2060	5.34	5.17	11.2	11.6	4.7	4.1	0.70	0.45
2080	6.79	6.62	14.4	13.6	6.0	4.8	0.89	0.62
2100	8.15	7.98	17.4	14.2	7.3	6.2	1.08	0.88

Table S2. *Anthropogenic radiative forcing (ARF) [Meinshausen et al., 2011], ARF – ARF(year = 1860), estimated injection rates, final injection rates*

c. A single simulation was then initiated for each aerosol, with initial injection rates as specified in table S2. After every 20 year interval, the simulation was stopped and the TOA-Imb was calculated for that time period. If there was significant deviation from zero (we adopted |mean(TOA-Imb)|> 0.25 W/m^2 as the criterion), then we recalculated the amount of injection required. The recalibration was conducted as follows: the TOA-RF at the end of the 20 year period (time = t_{20}) was calculated for the mean of the RCP8.5

ensemble, denote this R_{rcp}. The injection of aerosol at time t_{20} at rate I_{geo} produced TOA-Imb R_{geo} which we wish to be zero. Therefore an improved injection rate at t_{20} would be $I'_{geo} = I_{geo} \cdot R_{rcp}/(R_{rcp} - R_{geo})$. Additionally, at all specified timesteps after t_{20} ($t_n = t_{20}+20n$, n = 1,...), we modify the injection rate as such: $I'_{geo}(t_n) = I_{geo}(t_n) \cdot R_{rcp}/(R_{rcp} - R_{geo})$. After resetting the injection rates, we restarted the simulation from the start of the last time period. Final injection rates are given in table S2. We then used the final injection rates to run two more ensemble members for each aerosol

Section S3. Global/annual-mean net radiation and surface heat flux timeseries

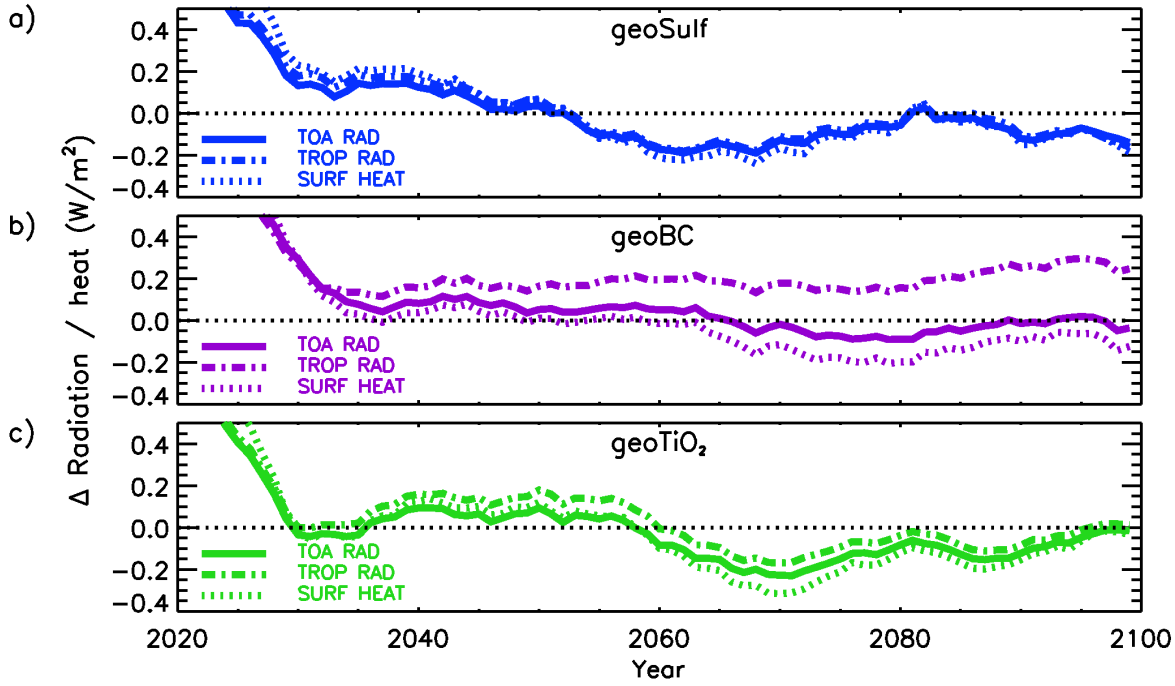

Figure S3. *10-year running-average global/annual-mean net radiation anomaly at the tropopause and TOA, and net-downward heat flux anomaly at the surface, with respect to piControl. Positive values indicate an increase in net downward flux*

Text S3. Figure S3 shows the global/annual-mean net radiation (positive downwards) at the tropopause and TOA with respect to the mean of the piControl simulation, and the net surface heat flux (radiative, sensible, & latent terms – positive downwards). This plot is used to show the significant difference in radiative perturbations between the tropopause and TOA in the geoBC experiment, leading to a net gain in radiative energy (kinetic energy is not considered here) in the troposphere in geoBC

Section S4. 2090s 550nm aerosol optical depth anomaly

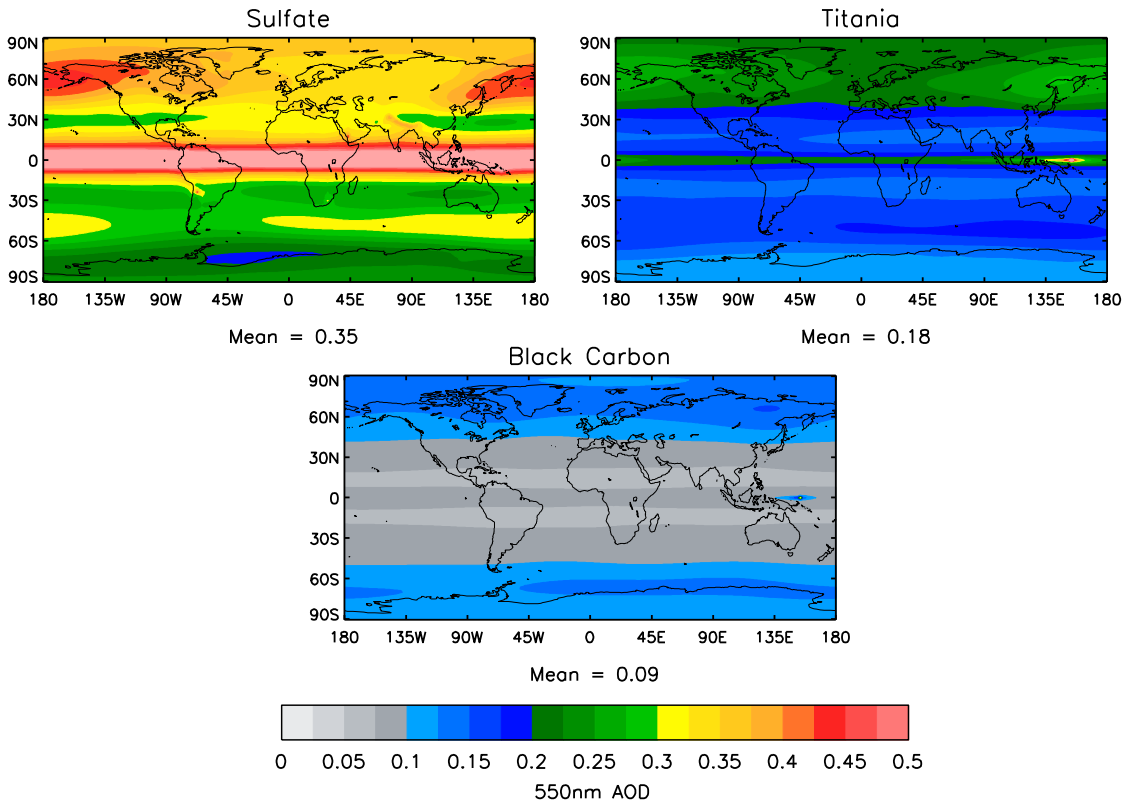

Figure S4. *Annual-mean 550nm optical depth anomaly for sulfate (geoSulf), titania (geoTiO$_2$) and black carbon (geoBC)*

Text S4. Figure S4 shows the aerosol optical depth anomaly. This clearly highlights the difference in latitudinal distributions, as also shown in Fig. 4 in the manuscript

Section S5. 2090s seasonal aerosol deposition anomaly

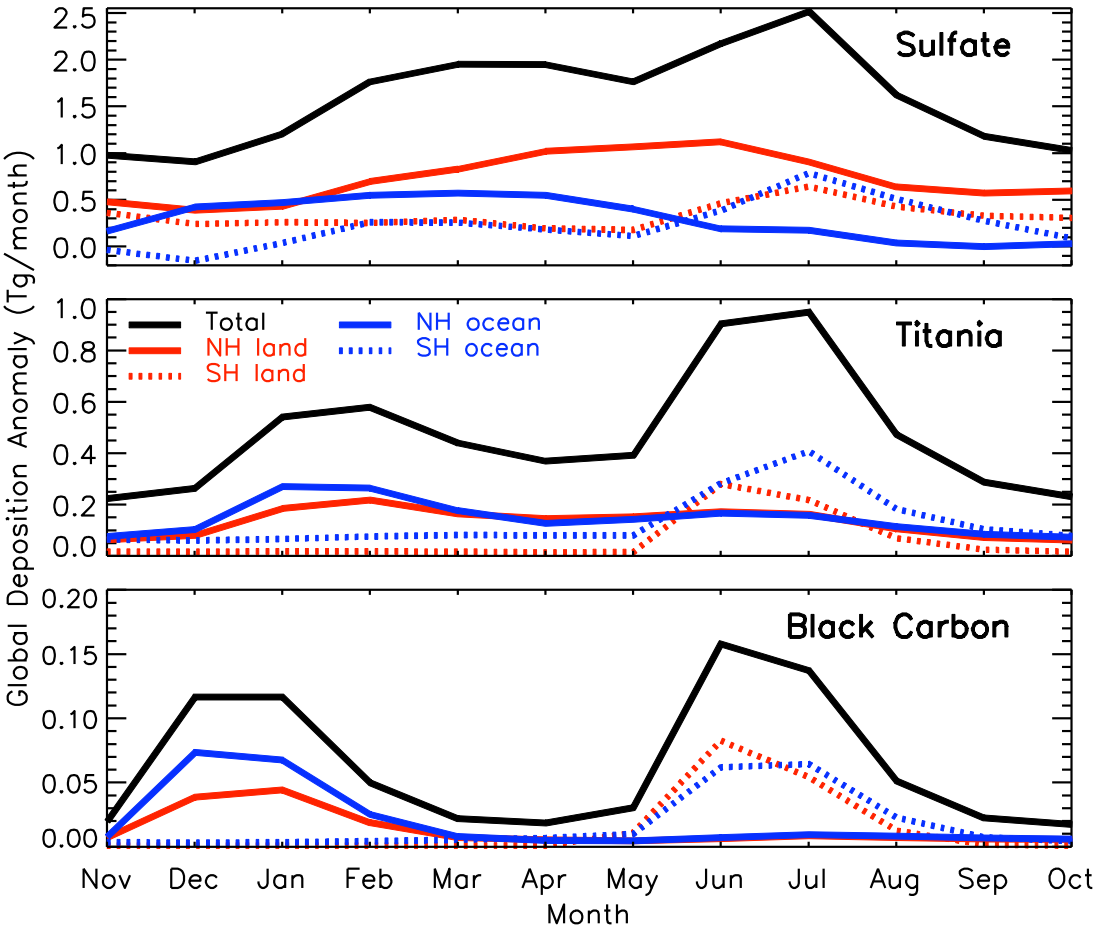

Figure S5. *Seasonal cycle of global/monthly-total aerosol deposition anomaly*

Text S5. 2090s seasonal aerosol deposition anomaly. This plot highlights the biannual deposition pattern for titania and BC (with aerosol deposited in the winter hemisphere), which is less apparent for sulfate. NH/SH refer to Northern Hemisphere and Southern Hemisphere respectively

Section S6. 2090s global-mean surface energy flux anomalies

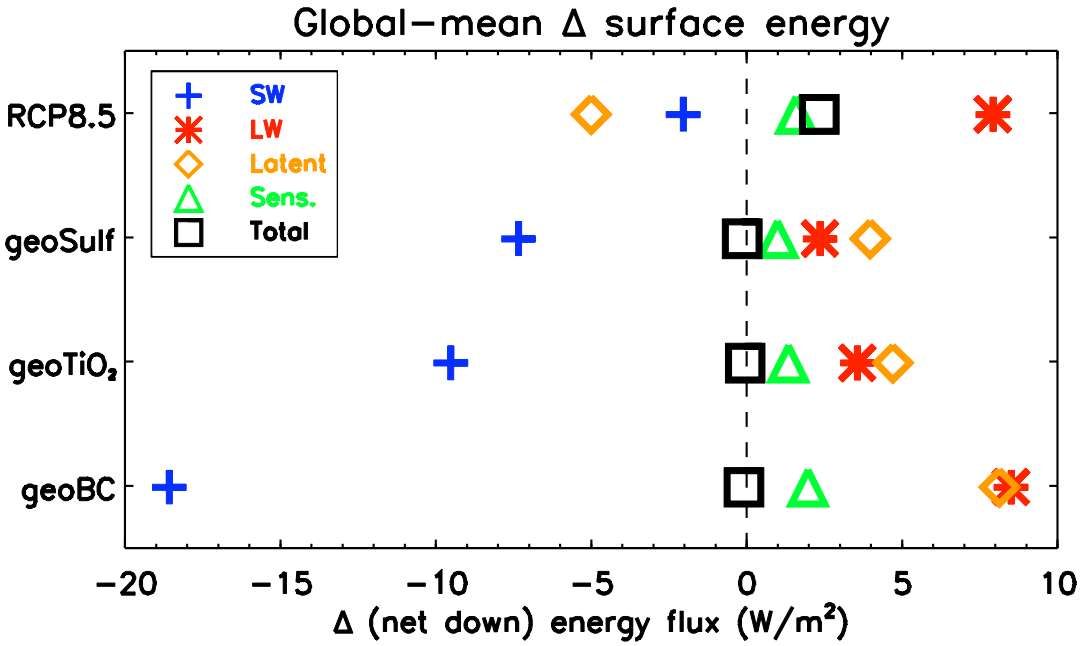

Figure S6. *2090's global/annual-mean net-downward energy flux anomalies at the surface (W/m^2). Calculated with respect to piControl*

Text S6. 2090's global/annual-mean net-downward energy flux anomalies at the surface (W/m^2). This plot shows the significant difference in surface SW forcing between the BC and the sulfate/ titania simulations

Section S7. 2090s Antarctic DJF sea-ice extent anomalies

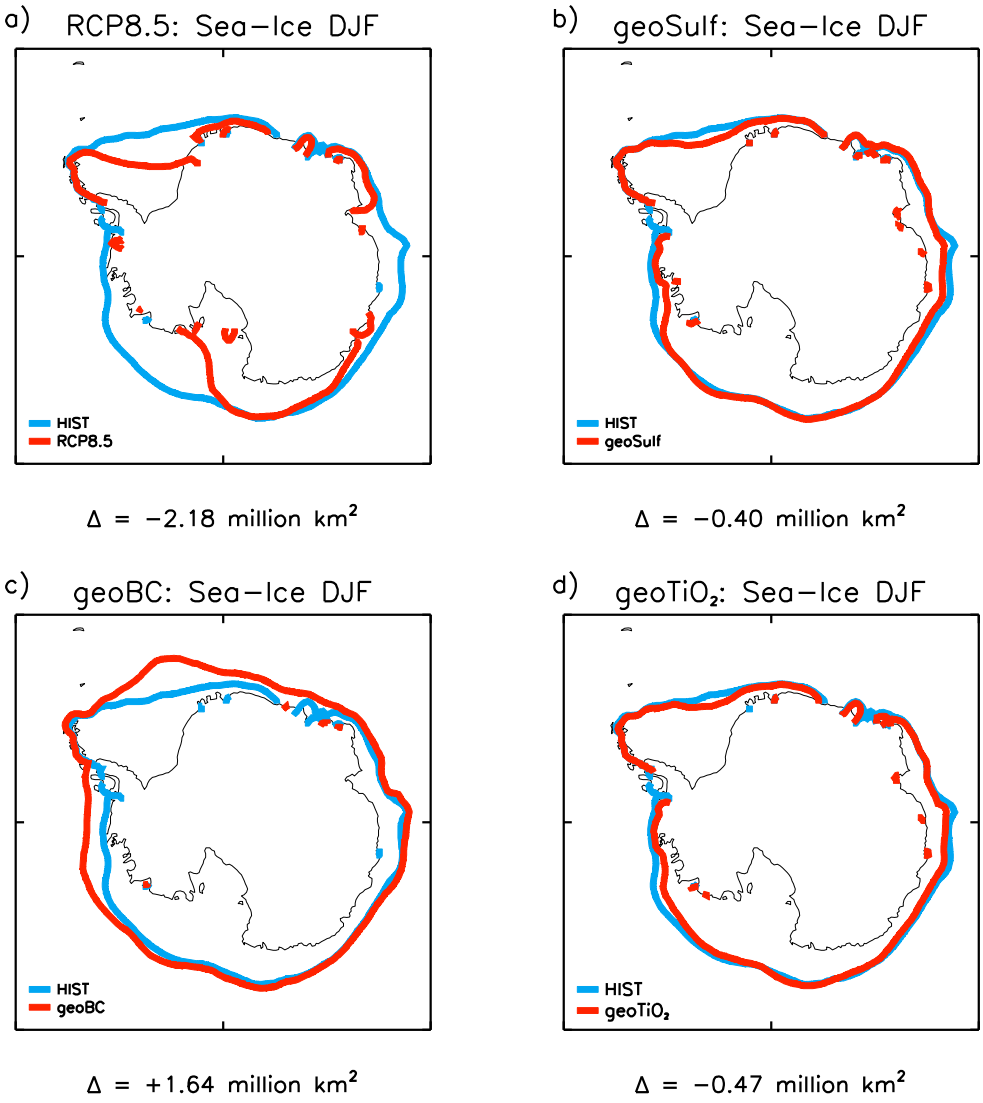

Figure S7. *DJF southern-hemisphere sea-ice edge plotted with the HIST extent*

Text S7. 2090s Antarctic DJF sea-ice extent anomalies plotted with the HIST extent. This plot can be compared with the NH equivalent (Fig.9) in the manuscript. As noted, SAI clearly maintains DJF sea-ice at approximately HIST levels, although geoBC exhibits an overcompensation

Section S8. 2090s geoengineering minus RCP8.5, 'aerosol-induced', zonal-mean temperature anomaly

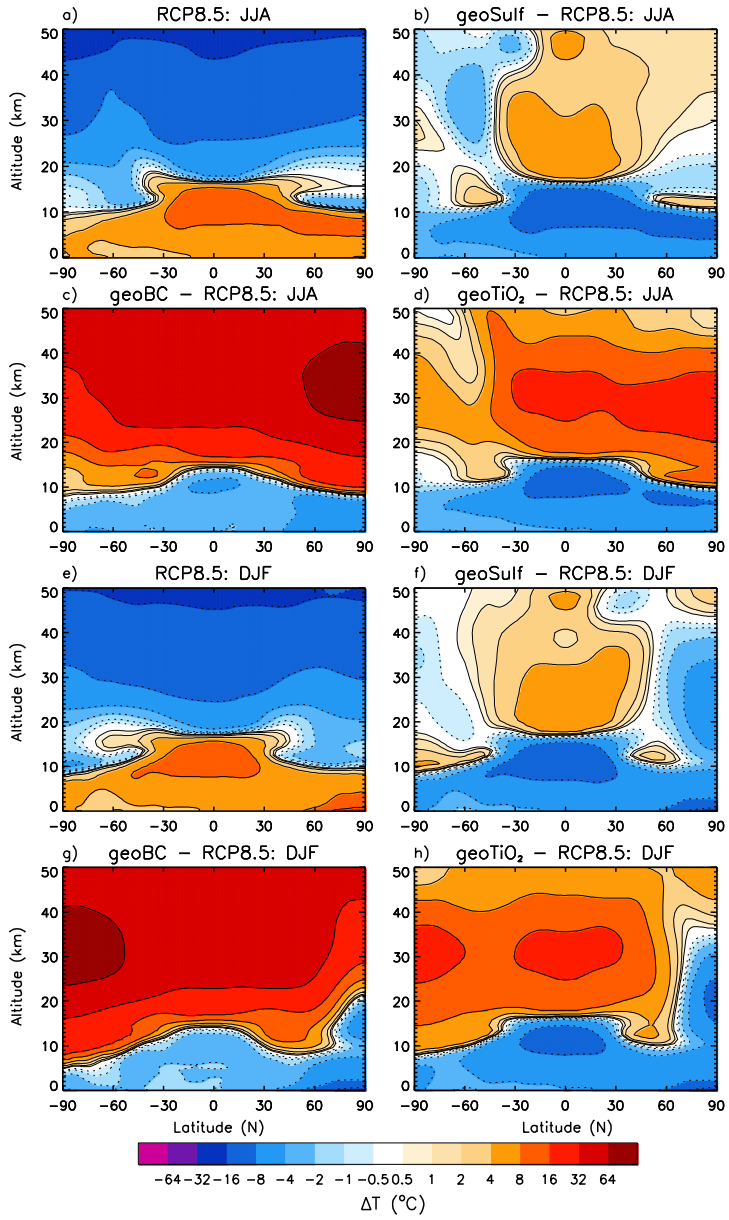

Figure S8. *JJA (top) and DJF (bottom) zonal-mean temperature anomaly with altitude, with respect to the HIST temperature profile for RCP8.5 (a,e), and with respect to RCP8.5 for geoSulf, geoBC and geoTiO$_2$*

Text S8. This plot shows the temperature changes induced by the aerosol layer, i.e. the 2090s temperature anomaly with respect to the baseline RCP8.5 2090s temperature. The peak aerosol-induced temperature changes are +76^{o}C, +7^{o}C, and +22^{o}C for geoBC, geoSulf and geoTiO2 respectively (as given in the manuscript).

Section S9. 2090s NH DJF zonal-mean zonal wind anomaly

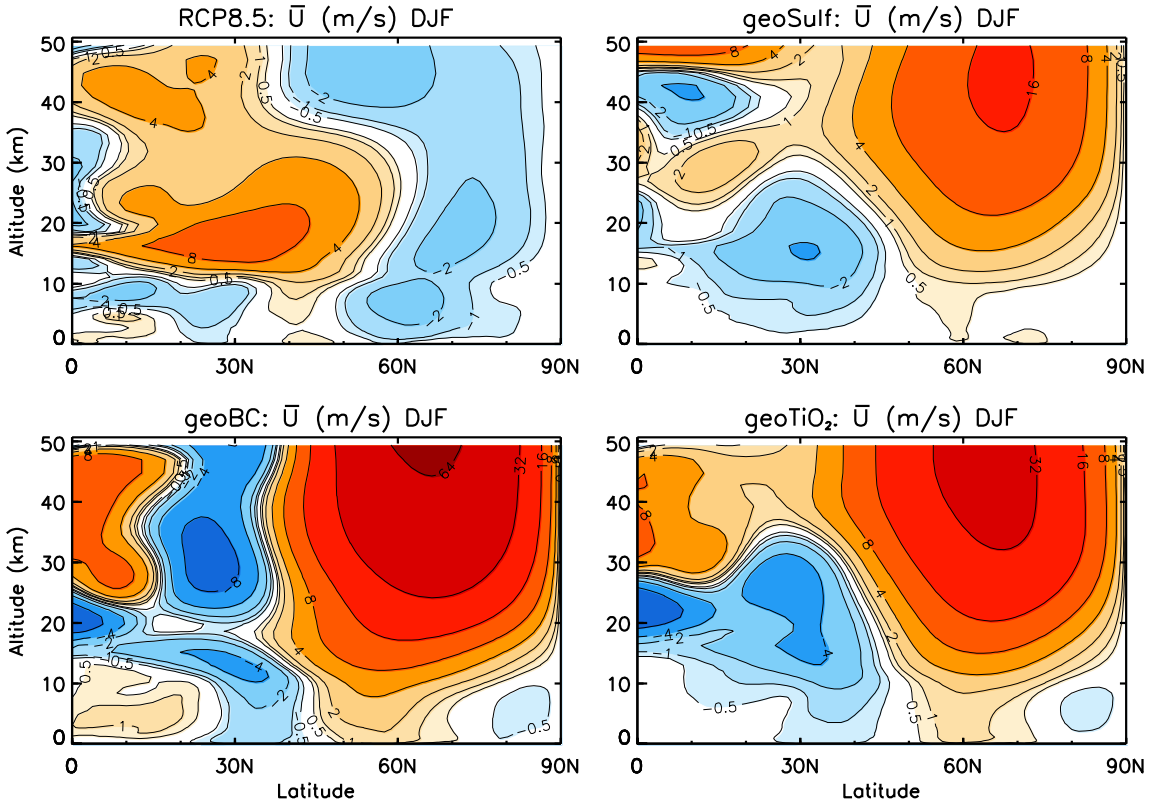

Figure S9. *DJF zonal-mean zonal wind anomaly with respect to HIST*

Text S9. This plot shows the NH DJF zonal wind anomaly (with respect to HIST) in the RCP8.5 and geoengineering simulations. The geoengineering simulations exhibit a strong increase in the strength of the polar vortex at ~60N

Section S10. Equatorial stratospheric zonal-mean zonal wind (QBO) fields

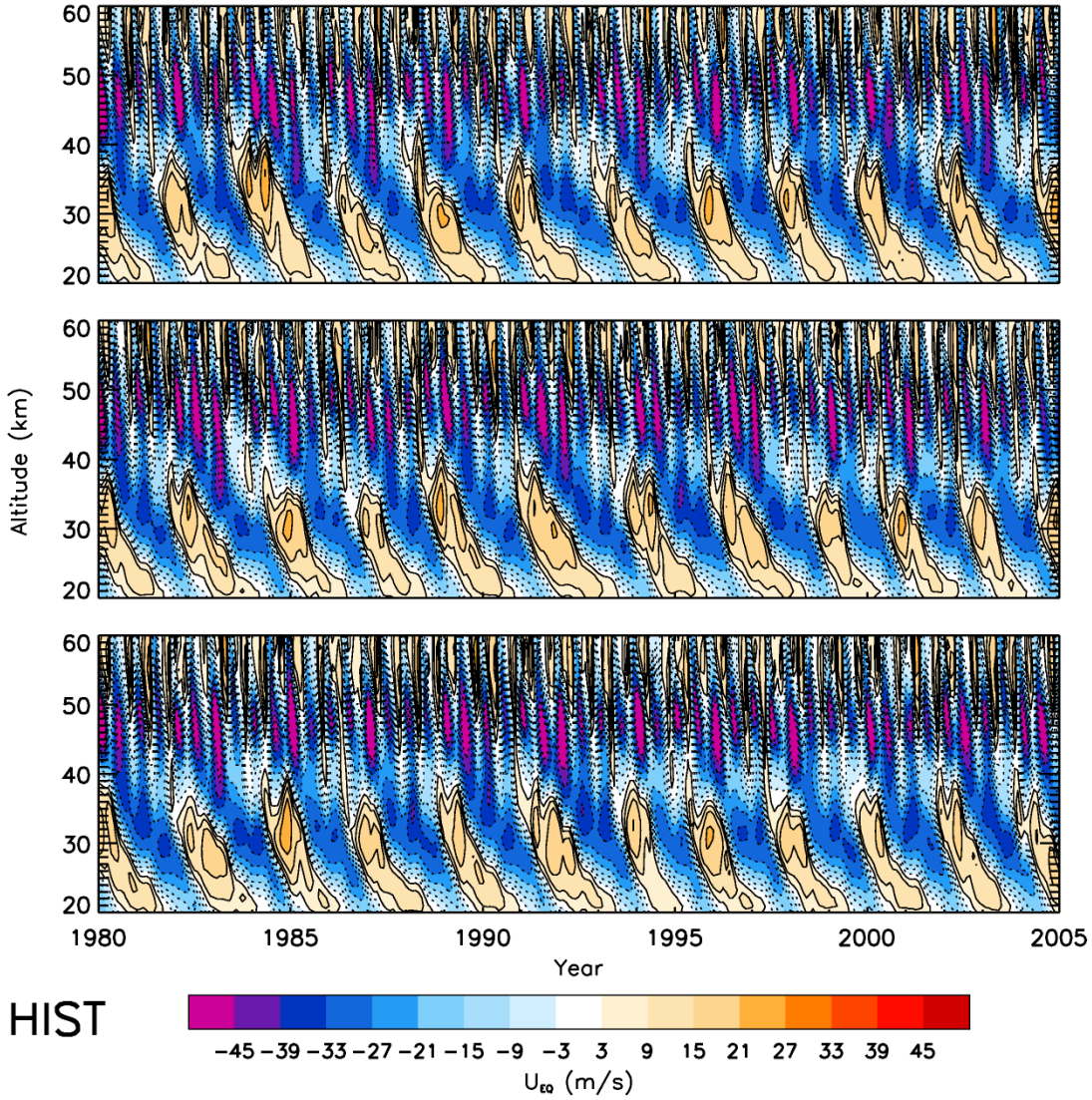

Figure S10. *Timeseries of equatorial (5°S-5°N) zonal-mean zonal wind profile (HIST - 3 ensemble members)*

Text S10. This plot shows the internally-forced QBO from the HIST-era ensemble

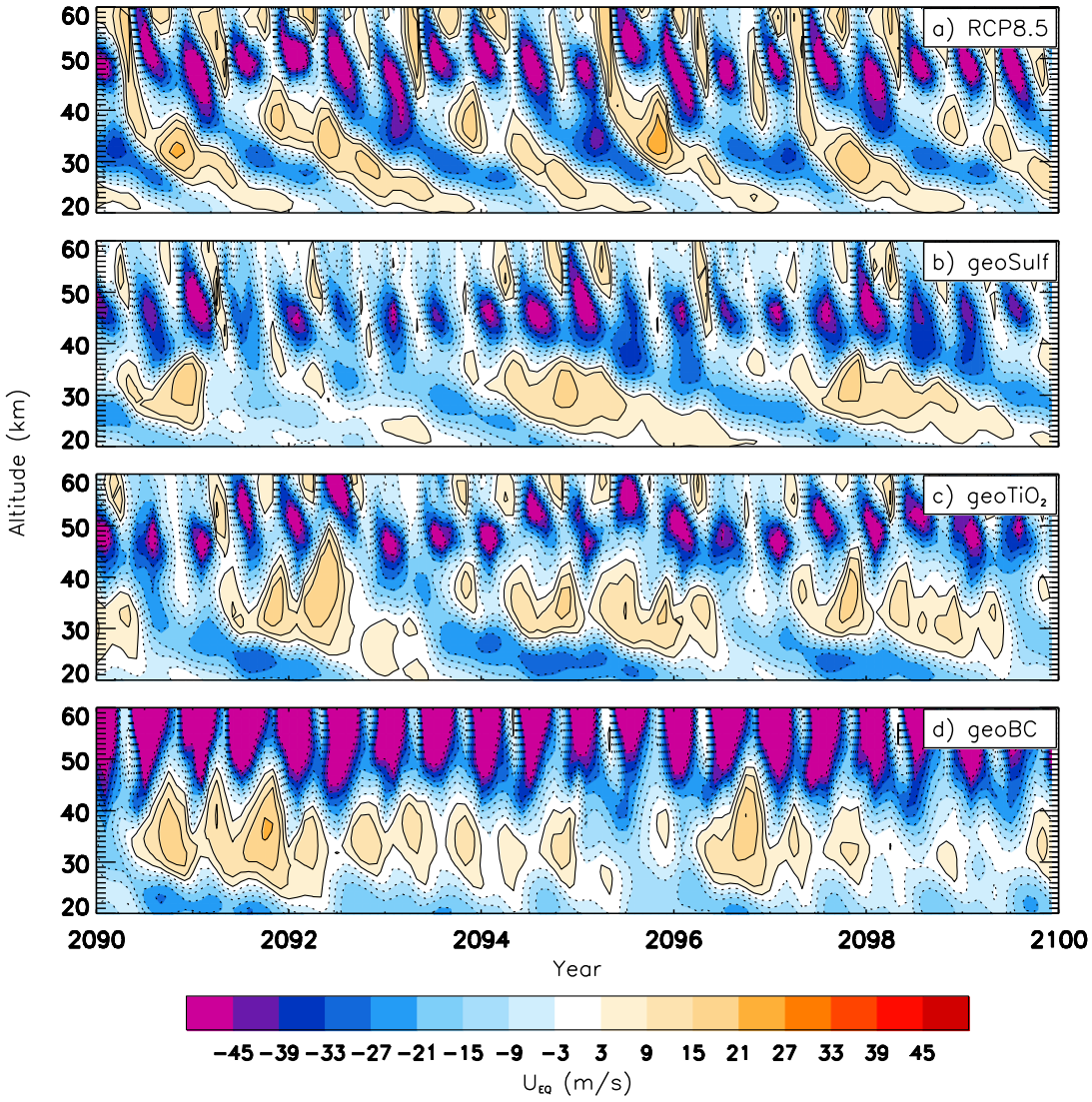

Figure S11a. *Timeseries of equatorial (5°S-5°N) zonal-mean zonal wind profile (2nd ensemble member)*

Text S11a. This plot is equivalent of Fig. 12 in the manuscript for the second member of each ensemble

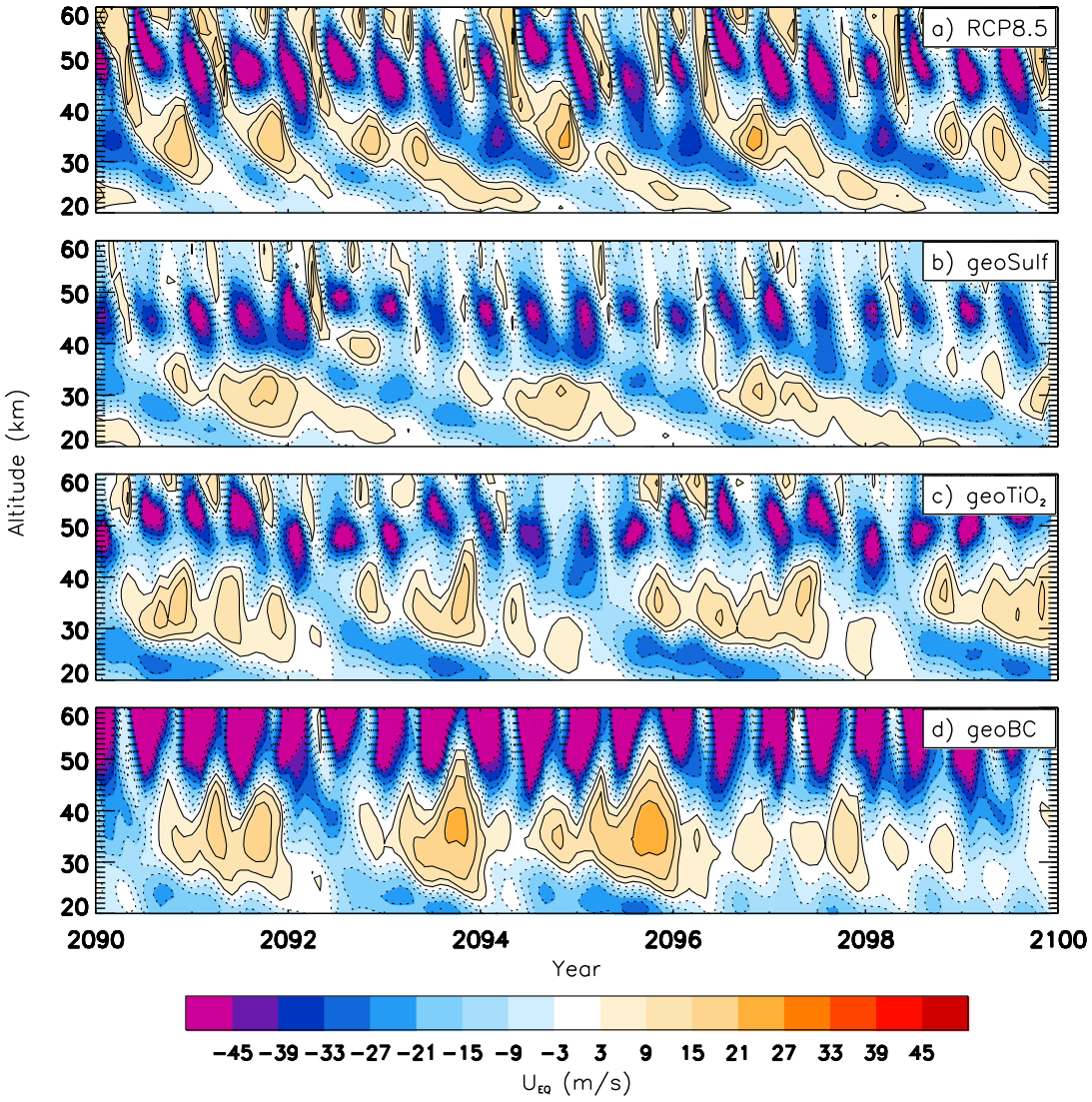

Figure S11b. *Timeseries of equatorial (5°S-5°N) zonal-mean zonal wind profile (3rd ensemble member)*

Text S11b. This plot is equivalent of Fig. 12 in the manuscript for the third member of each ensemble

Section 11. Global-mean thermosteric sea-level time-series

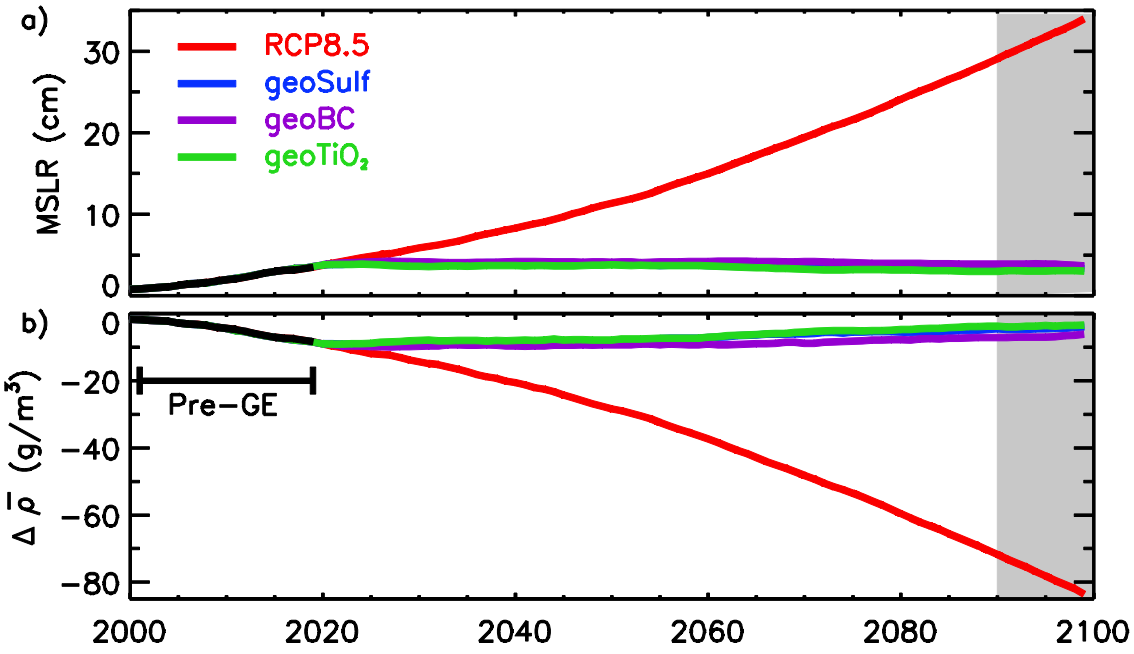

Figure S12. *Timeseries of global thermosteric sea-level rise, calculated using changes in oceanic temperature and salinity. (Top) Global mean thermosteric sea-level rise (bottom) Global mean oceanic density anomaly*

Text S12. This plot shows the global-mean sea-level change due to oceanic temperature and salinity perturbations. The oceanic density is calculated from salinity and temperature using the UNESCO equation of state